Asymptotics of dynamic lattice Green's functions

A. L. Vanel*, R. V. Craster, D. J. Colquitt[1], M. Makwana[2]

Department of Mathematics, Imperial College London, London SW7 2AZ, UK

Abstract

In the study of periodic problems it is natural and commonplace to use Fourier transforms to obtain explicit lattice Green's functions in the form of multidimensional integrals. Considerable physical information is encapsulated within the Green's function and our aim is to extract the behaviour near critical frequencies by creating connections with multiple-scale homogenisation methods recently applied to partial differential equations. We show that the integrals naturally contain two-scales, a short-scale on the scale of the lattice and a long-scale envelope. For pedagogic purposes we first consider the well-known two dimensional square lattice, followed by the three dimensional cubic lattice. The features we uncover, and the asymptotics, are generic for many lattice structures. Finally we consider a topical three dimensional example from structural mechanics showing dynamic anisotropy, that is, at specific frequencies all the energy is directed along specific characteristic directions.

Keywords: Homogenisation, Lattice Green's Function, Asymptotics

1. Introduction

The Green's function for a discrete lattice is a fundamental building block for many problems in solid state physics [19], structural mechanics [30, 33] and more generally in lattice dynamics [6] and has a long and distinguished history. Lattice Green's functions have therefore, unsurprisingly, been the focus of intense analysis over the years and the book by [17] contains a vast amount of useful information as do the earlier works of [23, 26, 27]. The focus in this article is in relating the asymptotics of this classical lattice Green's function, and modern variants, with the asymptotic representations that emerge from an

*Corresponding author

Email addresses: alice.vanel13@imperial.ac.uk (A. L. Vanel), r.craster@imperial.ac.uk (R. V. Craster), d.colquitt@liverpool.ac.uk (D. J. Colquitt), mehul@multiwave.ch (M. Makwana)

[1]Present address: Department of Mathematical Sciences, University of Liverpool, Liverpool L69 7ZL, UK

[2]Present address: Multiwave Technologies AG, Rennweg 39, 5303 Würenlingen, Switzerland

alternative viewpoint which is to homogenise the physical system using multiple scales at the outset and then analyse the homogenised system [15].

Homogenisation is usually limited to low-frequency and long-wave excitation whereby the typical wavelength is much greater than the interparticle spacing and is therefore of limited interest in lattice dynamics: many of the more interesting effects occur at higher frequencies. One can utilise the ideas of homogenisation - the techniques of multiple scales - for periodic, or nearly periodic, media provided one is close to standing wave frequencies, that is, at the band-gap edges or the edges of the Brillouin zone [15] (see also [4, 5] for similar approaches to the Schrödinger equation); although this requirement can be relaxed using Brillouin zone folding. This results in a short-scale, potentially rapidly varying, solution modulated by a long-scale envelope function that satisfies a partial differential equation with asymptotic solutions found for propagating and localised solutions [25].

The usual setting of, say, the vibrations of identical masses on a square lattice with nearest neighbour interactions leads to a partial difference equation for the displacements $y_{n,m}$ at a lattice position (n, m); assuming fixed frequency, and excitation at a single site, one can use Fourier transforms to rapidly obtain the Green's function as an inverse Fourier integral. A review of this material is in [28], for the square lattice, which illustrates the various approaches typically used to evaluate that integral that revolve around analysing the far-field when $|n|, |m| \gg 1$. For the far field the Fourier integrals naturally lend themselves to stationary phase techniques either directly [20], or to ingenious manipulations of the integral [23], or in two-dimensional settings one can sometimes reduce the problem to the analysis of special functions [10, 35]; a simplification of $n = \pm m$, along the diagonals, further aids matters. [28] concentrates upon frequencies for which waves propagate, and the complementary situation with localised states, from this viewpoint, are treated in [29] and [13]. In essence to evaluate the integral asymptotically one requires a small (or large) parameter that is facilitated by taking the far field, or alternatively entering the arena of special functions and approximating those.

It is natural to query how the two approaches, homogenisation and Green's function integrals, are connected and consistent with each other: It should be possible to extract the multiple-scales homogenisation asymptotics from the Green's function integrals and indeed given the importance of the Green's function approach it is important to be able to do so. The technique provides a different way of interpreting the Fourier integrals that appear by isolating the short-scale rapid oscillations from a longer scale solution that can then be analysed more easily and this approach does not rely upon far-field or stationary phase techniques.

We are also motivated by wave phenomena in structured continuum mechanics that show strong directional anisotropy when forced close to specific frequencies and this behaviour is observed in optics for photonic crystals [2, 9], in microwave experiments, simulations and asymptotics involving arrays of dielectric fibres [8], and in elastic lattices and frames [12]. For two-dimensional mass-spring lattices, [22], showed strongly directional cross-like responses close

to critical frequencies and more recent authors [3, 31, 32] have demonstrated and investigated this behaviour further with [14] connecting the strong anisotropy in these model discrete systems to the continuum observations and interpreting this in terms of a change in character of the effective equations from elliptic to hyperbolic; the highly directional behaviour then being along the characteristics of the hyperbolic effective equations. The vast majority of this work is, due to computational expense, and difficulties in terms of experiments, confined to two-dimensions and a natural question is whether similar strong localisation along beams occurs in three-dimensions. We provide the appropriate analysis here, together with supporting numerical simulations, for the discrete model systems and then extend it to an elastic frame model to demonstrate the utility of our approach.

In this article we begin by illustrating the methodology on the classical square lattice for two-dimensions in section 2, then move to the three-dimensional cubic lattice in section 3. A topical example from the literature of elastic frames is then used in section 4 to illustrate that the phenomena we discuss are widespread and that our interpretation and analysis is more widely applicable. We draw together some concluding remarks in section 5.

2. The square lattice

We consider the canonical two-dimensional mass-spring lattice [7] of identical masses placed upon a square lattice, with point forcing at $n = m = 0$. Assuming harmonic wave forcing with frequency Ω the displacements $y_{n,m}$ are given by

$$y_{n+1,m} + y_{n-1,m} + y_{n,m+1} + y_{n,m-1} + (\Omega^2 - 4)y_{n,m} = \delta_{0,0} \tag{1}$$

for integer n, m and $\delta_{0,0}$ as the Kronecker delta; this has been non-dimensionalised so the spring constant and mass are both unity.

In the absence of forcing one can consider Bloch solutions of the form $y_{n+N,m+M} = \exp(i[\kappa_1 N + \kappa_2 M])y_{n,m}$ for integer N, M and $\boldsymbol{\kappa} = (\kappa_1, \kappa_2)$ is the Bloch wavevector representing a phase shift as one moves from one mass to another. The dispersion relation between the Bloch wavenumbers and frequency is

$$D(\Omega, \kappa_1, \kappa_2) = \Omega^2 - 4 + 2(\cos\kappa_1 + \cos\kappa_2) = 0. \tag{2}$$

The dispersion relation naturally holds the key to understanding many of the physical phenomena present. It is conventional, given the periodicity, to represent the dispersion properties by using the irreducible Brillouin zone [7] and by plotting the dispersion curves around the edges of the zone, see figure 1(a); some care is however required as pointed out in [14] and we also show the full isofrequency contours in figure 1(b).

The Bloch wavevector characterises the phase shift from one mass to its neighbour and, importantly, there exist standing waves where the mass displacement is either perfectly in-phase or out-of-phase with its neighbour: these

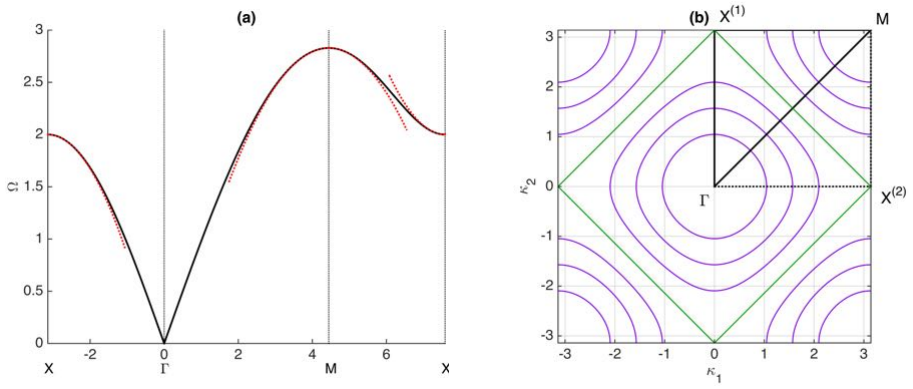

Figure 1: The dispersion curve (a) and isofrequency contours (b) for the square lattice (1). Panel (a) the dispersion relation plotted along the edges of the irreducible Brillouin zone. Panel (b) the isofrequency contours (purple) of (1) in $\boldsymbol{\kappa}$-space with the black triangle ΓXM (with $X^{(1)} = X$) showing the irreducible Brillouin zone. The tilted square contour corresponding to the standing wave frequency $\Omega_0^2 = 4$ is shown in green.

lie at the vertices of the irreducible Brillouin zone, i.e., at points Γ, X, M in Fig. 1(a). These are now classical results, as is the Fourier solution to (1)

$$y_{n,m} = \frac{1}{(2\pi)^2} \int_{-\pi}^{\pi} \int_{-\pi}^{\pi} \frac{\exp[-i(k_1 n + k_2 m)]}{D(\Omega, k_1, k_2)} \mathrm{d}k_1 \mathrm{d}k_2. \tag{3}$$

The asymptotic approach usually utilised is to look in the far field and to take $|n|, |m| \gg 1$ and then to analyse this in the language of the method of stationary phase, see [28] and the literature cited therein. Our approach is complementary and instead aims to analyse this integral in the neighbourhood of certain frequencies via a perturbation method, that isolates short-scale and long-scale behaviour, and then to demonstrate that this, at least for these integrals, is equivalent to the multiple scales homogenisation approach of [15].

We consider asymptotics based around frequencies at the edges of the Brillouin zone shown in figure 1 and explicitly consider them at the wavevector points M, X in turn; the long-wave low frequency asymptotics at Γ are straightforward and will not be considered here.

2.1. Asymptotics near M

At M the wavevector in $\boldsymbol{\kappa}$ space is (π, π) and the standing wave frequency is $\Omega_0 = \sqrt{8}$. We perturb in frequency space with the Ansatz

$$\Omega^2 \sim \Omega_0^2 + \epsilon^2 \Omega_2^2 \tag{4}$$

with $0 < \epsilon \ll 1$. In the integral (3) we make the change of variables $k_1 = \pi + \epsilon\alpha$, $k_2 = \pi + \epsilon\beta$, using the periodicity of the integral and thereby centring the region

of integration at M. We obtain the following, after taking the limit $\epsilon \to 0$,

$$y_{n,m} = \frac{\exp[-i\pi(n+m)]}{(2\pi)^2} \int_{-\infty}^{\infty}\int_{-\infty}^{\infty} \frac{\exp[-i(\alpha\eta_1+\beta\eta_2)]}{\alpha^2+\beta^2+\Omega_2^2} \mathrm{d}\alpha\mathrm{d}\beta + \mathcal{O}(\epsilon), \qquad (5)$$

where we introduce a long-scale variable $\boldsymbol{\eta} = (\eta_1, \eta_2) = \epsilon(n, m)$. The choice of Ansatz in (4), and scalings in k_1, k_2, are motivated to balance terms such that at $\mathcal{O}(1)$ an integral naturally emerges as (5). This integral has naturally separated into a short-scale oscillatory component that we denote as $Y_{n,m}$, and $Y_{n,m} = \exp[-i(n+m)\pi]$, and a long-scale component $f(\boldsymbol{\eta})$ as the remaining Fourier integral; that is $y_{n,m} = Y_{n,m}f(\boldsymbol{\eta}) + O(\epsilon)$. The integral in (5) is standard and

$$f(\boldsymbol{\eta}) = \begin{cases} \frac{1}{2\pi} K_0\left(\sqrt{\Omega_2^2} r\right) & \text{if} \quad \Omega_2^2 > 0 \\ \frac{i}{4} H_0^{(1)}\left(\sqrt{-\Omega_2^2} r\right) & \text{if} \quad \Omega_2^2 < 0 \end{cases}, \qquad (6)$$

in terms of the modified Bessel function K_0 and the Hankel function $H_0^{(1)}$ [1] where $r = (\eta_1^2 + \eta_2^2)^{1/2}$. As Ω_2^2 multiplies the perturbation away from the standing wave frequency, see (4), then when it is negative we have propagation and, conversely, when it is positive we have a decaying solution.

Numerical simulations for comparison with the asymptotics are found by truncating the infinite system (1) then using perfectly matched layers (PML) on the boundaries [25] to mimic an infinite domain. Alternatively, one can use Fast Fourier Transforms (FFTs) to directly evaluate the integrals and this latter approach is more convenient in three dimensions. However, the integrand is singular for some κ. To regularise, we add a small imaginary part, so the denominator becomes $D(\boldsymbol{k}, \Omega) + \varepsilon i$. The typical value used for ε is $5 \cdot 10^{-3}$. Both methods are used in the comparisons and we state which is used in the appropriate figure captions. Other approaches are used in, say, [21] and FFT or truncation with PML are not the only routes to evaluating the various integrals that arise.

In the propagating region, figure 2(a) illustrates long-scale isotropic behaviour with a decaying oscillatory envelope as expected from the Hankel function (6), and in Fig. 2(b) we see the local short-scale oscillations. Panel (c) of the same figure illustrates antiperiodicity on the short-scale along $m = 0$, where $Y_{n,0} = (-1)^n$, and compares numerics with asymptotics showing almost perfect agreement.

The high frequency homogenisation of [15] also generates these solutions by adopting Ansätze of the form

$$y_{n,m} = y_{0,n,m} + \epsilon y_{1,n,m} + \epsilon^2 y_{2,n,m} + \mathcal{O}(\epsilon^3), \qquad \Omega^2 = \Omega_0^2 + \epsilon\Omega_1^2 + \epsilon^2\Omega_2^2 + \mathcal{O}(\epsilon^3) \quad (7)$$

in the difference equation (1). Introducing the variable $\boldsymbol{\eta} = (\eta_1, \eta_2)$, a natural separation of scales emerges and yields a hierarchy of equations in powers of ϵ. At leading order we obtain the standing wave frequency $\Omega_0^2 = 8$, and a separation of scales at leading order with $y_{0,n,m} = Y_{n,m}f(\boldsymbol{\eta})$, where f is governed by a

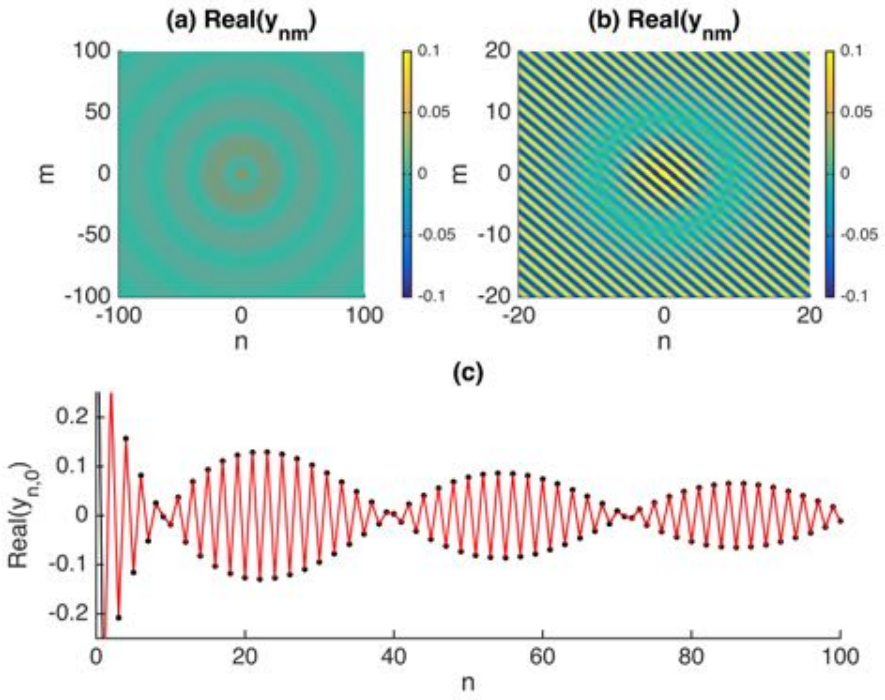

Figure 2: The field excited just below the standing wave frequency, at $\Omega = \sqrt{8 - 0.01}$, at point M of the Brillouin zone. These are from the numerical simulation of a discrete mass-spring square periodic lattice, excited at the origin, for 1001x1001 masses surrounded with a 100 mass deep layer of PML. Panel (a) shows the full numerical solution that oscillates and decays as expected. Panel (b) shows detail near the origin with the short-scale antiperiodicity in both m- and n-directions shown. Panel (c) shows a line plot along the axis $m = 0$ with displacements from the numerics (black dots) and asymptotics from equation (6) (red lines).

partial differential equation on the long-scale:

$$f_{\eta_1\eta_1}(\boldsymbol{\eta}) + f_{\eta_2\eta_2}(\boldsymbol{\eta}) - \Omega_2^2 f(\boldsymbol{\eta}) = -\delta(\eta_1)\delta(\eta_2) \tag{8}$$

which has solution (6).

2.2. Asymptotics near X

The wavenumber at X $(= X^{(1)})$ has, from the symmetries of the irreducible Brillouin zone, a related point $X^{(2)}$ at $(\pi, 0)$ (see figure 1(b)) and the standing wave frequency is $\Omega_0 = 2$. By the periodicity of the Fourier integral, there are also two other related points but $X^{(1)}$ is equivalent to $X^{(3)} = (0, -\pi)$, and $X^{(2)}$ to $X^{(4)} = (-\pi, 0)$ and they need not be considered further.

We consider the $X^{(1)}$ point in detail and just note the main results for $X^{(2)}$. We again adopt the Ansatz (4) but now use periodicity and centre the region of integration at $X^{(1)}$ in (3) and make the change of variables $k_1 = \epsilon\alpha$, $k_2 = \pi + \epsilon\beta$

to obtain the following integral taking the limit $\epsilon \to 0$

$$y_{n,m} = \frac{\exp[-im\pi]}{(2\pi)^2} \int_{-\infty}^{\infty}\int_{-\infty}^{\infty} \frac{\exp[-i(\alpha\eta_1 + \beta\eta_2)]}{-\alpha^2 + \beta^2 + \Omega_2^2} \mathrm{d}\alpha\mathrm{d}\beta + \mathcal{O}(\epsilon), \tag{9}$$

after setting $\boldsymbol{\eta} = (\eta_1, \eta_2) = \epsilon(n, m)$. This has isolated the two scales yielding on the short-scale an oscillatory component $Y_{n,m} = \exp[-im\pi]$ and on the long-scale an integral, which has solution

$$f(\boldsymbol{\eta}) = \begin{cases} AH_0^{(1)}\left(\sqrt{\rho^2\Omega_2^2}\right) & \text{if} \quad \rho^2\Omega_2^2 > 0 \\ BK_0\left(\sqrt{-\rho^2\Omega_2^2}\right) & \text{if} \quad \rho^2\Omega_2^2 < 0 \end{cases}, \tag{10}$$

where $\rho^2 = \eta_1^2 - \eta_2^2$, A and B are constants, $H_0^{(1)}$ is the Hankel function and K_0 the modified Bessel function. It is worth noticing that there is a logarithmic singularity where $\eta_1 = \pm\eta_2$, on the diagonals, hence the solution is divided into pieces valid in different quadrants as shown in Fig. 3(b) and the inset. The Hankel function solutions are substantially larger in amplitude than the K_0 solutions that rapidly become exponentially decaying as $|m|, |n|$ increase.

For $X^{(2)}$, we use hatted decoration to distinguish them from those near $X^{(1)}$, we obtain the Fourier solution

$$\hat{y}_{n,m} = \frac{\exp[-in\pi]}{(2\pi)^2} \int_{-\infty}^{\infty}\int_{-\infty}^{\infty} \frac{\exp[-i(\alpha\eta_1 + \beta\eta_2)]}{\alpha^2 - \beta^2 + \Omega_2^2} \mathrm{d}\alpha\mathrm{d}\beta + \mathcal{O}(\epsilon), \tag{11}$$

for which the long-scale integral has solution

$$\hat{f}(\boldsymbol{\eta}) = \begin{cases} \hat{A}H_0^{(1)}\left(\sqrt{-\rho^2\Omega_2^2}\right) & \text{if} \quad \rho^2\Omega_2^2 < 0 \\ \hat{B}K_0\left(\sqrt{\rho^2\Omega_2^2}\right) & \text{if} \quad \rho^2\Omega_2^2 > 0 \end{cases}, \tag{12}$$

for $\hat{A}$, $\hat{B}$ constants and the short-scale is $\hat{Y}_{n,m} = \exp[-in\pi]$.

The full solution close to the frequency $\Omega = 2$ is the sum of those at $X^{(1)}$ and $X^{(2)}$. We notice that depending on the sign of Ω_2^2, the solution will differ in each quadrant, labelled 1,2,3 and 4 on figures 3(b) and 4(b), since $\rho^2 > 0$ in 2 and 4 and $\rho^2 < 0$ in 1 and 3. The microscale part of the solution $Y_{n,m} = (-1)^m$ is antiperiodic (resp. periodic) in the m-direction (resp. n-), whereas $\hat{Y}_{n,m} = (-1)^n$ has the opposite behaviour. The Hankel functions dominate on the long-scale and hence one can identify the dominant behaviour in each quadrant and, depending on the sign of Ω_2^2, the associated short-scale behaviour; this gives the very distinctive behaviour shown from frequencies above and below the frequency $\Omega = 2$ (c.f. figures 3 and 4).

Numerical simulations for $\Omega_2^2 < 0$ and $\Omega_2^2 > 0$ are shown in figures 3 and 4 respectively. Both figures illustrate the high dynamic anisotropy due to the logarithmic singularity along the diagonals with energy propagating mainly along

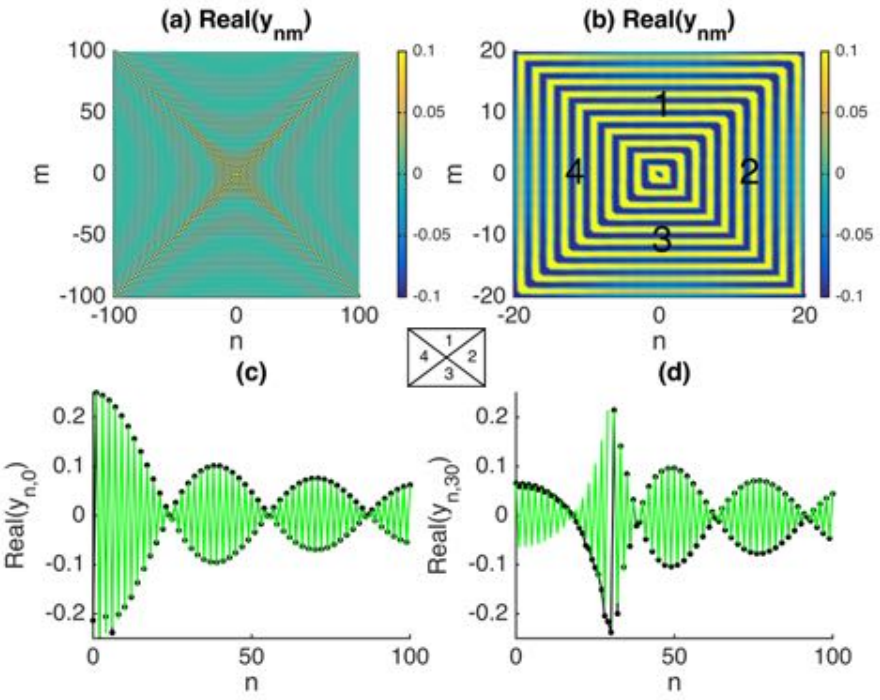

Figure 3: The field excited by a source at frequency $\Omega = \sqrt{4 - 0.01}$ at point X of the Brillouin zone. Panels (a) & (b) show a diagonal cross for a discrete mass-spring square periodic lattice excited at the origin for 1001x1001 masses surrounded with a 100 mass deep layer of PML. The zoomed-in picture in panel (b) reveals the antiperiodicity in m-direction and periodicity in n-direction in quadrants 2 and 4 and the complementary behaviour in quadrants 1 and 3. Panels (c) & (d) show in-phase and out-of phase masses displacement (black dots) along n, (c) along the line $m = 0$, (d) along the line $m = 30$. The asymptotics (green lines) emerge from (10) and (12).

the rays where $\rho^2 = 0$ in panel (a) of both figure 3 and 4. Panel (b) in both figures 3 and 4 show the detail of the behaviour near the origin and the predicted short-scale response is clearly observed. Panels (c) and (d) illustrate the excellent agreement between numerics and the asymptotics in terms of Hankel functions. The line plot along n at $m = 30$ in the panels (d) shows the discontinuity at $n = m$ when masses change from being in-phase to being out-of-phase with their neighbours.

We again return to the homogenisation technique of [15], with the Ansatz (7) for the point $X^{(1)}$, where the envelope function satisfies the Klein-Gordon equation,

$$f_{\eta_1\eta_1}(\boldsymbol{\eta}) - f_{\eta_2\eta_2}(\boldsymbol{\eta}) + \Omega_2^2 f(\boldsymbol{\eta}) = \delta(\eta_1)\delta(\eta_2). \tag{13}$$

Equation (13) is hyperbolic and has solution (10). For the point $X^{(2)}$, the

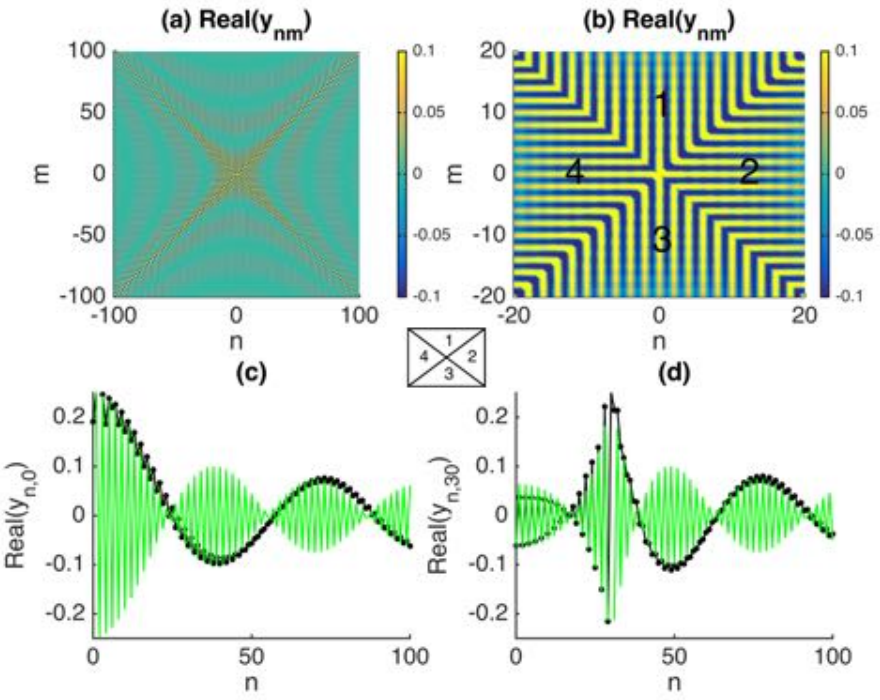

Figure 4: The field excited by a source at frequency $\Omega = \sqrt{4 + 0.01}$ at point X of the Brillouin zone. Panels (a) & (b) show a diagonal cross for a discrete mass-spring square periodic lattice excited at the origin for 1001x1001 masses surrounded with a 100 mass deep layer of PML. The zoomed-in picture on panel (b) reveals the antiperiocity in n-direction and periodicity in m-direction in quadrants 2 and 4 and the complementary behaviour in quadrants 1 and 3. Panels (c) & (d) show in-phase and out-of phase masses displacement (black dots) along n, (c) along the line $m = 0$, (d) along the line $m = 30$. The asymptotics (green lines) emerge from (10) and (12).

partial differential equation that ensues is

$$-\hat{f}_{\eta_1\eta_1}(\boldsymbol{\eta}) + \hat{f}_{\eta_2\eta_2}(\boldsymbol{\eta}) + \Omega_2^2\hat{f}(\boldsymbol{\eta}) = \delta(\eta_1)\delta(\eta_2), \tag{14}$$

and has solution (12).

The square lattice has, as mentioned earlier, been of interest in its own right [28] and recently for the highly directional anisotropy [3, 31, 32] see also [22]; the exact and simple asymptotic procedure and solutions shed light and aid interpretation of those results.

3. The cubic lattice

For a three-dimensional cubic-primitive lattice (henceforth cubic lattice), constructed from masses and springs, with point forcing at $m = n = p = 0$, the

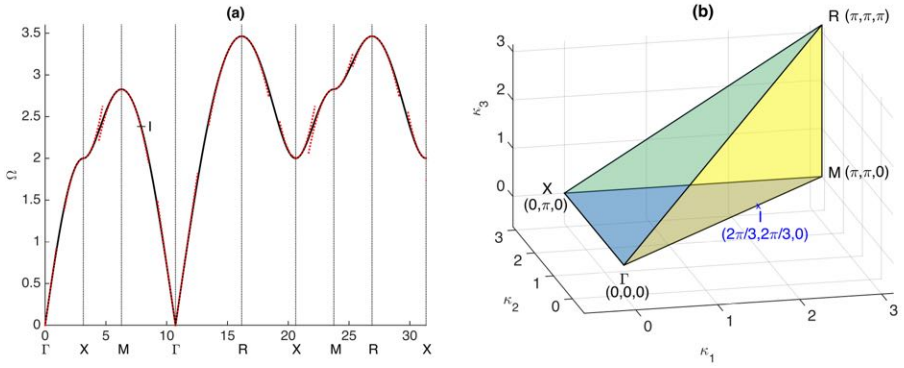

Figure 5: The Dispersion curve for a 3D monoatomic cubic lattice on panel (a) plotted around the edges of the irreducible Brillouin zone shown in panel (b). The red dotted lines on panel (a) are asymptotics from high frequency homogenisation theory.

analogous equation to (1) for the discrete field $y_{m,n,p}$ is

$$y_{m+1,n,p} + y_{m-1,n,p} + y_{m,n+1,p} + y_{m,n-1,p} + y_{m,n,p+1} + y_{m,n,p-1} + (\Omega^2 - 6)y_{m,n,p} = \delta_{0,0,0} \quad (15)$$

with frequency Ω and $\delta_{0,0,0}$ as the Kronecker delta. The dispersion relation relating Bloch wavenumber $\boldsymbol{\kappa} = (\kappa_1, \kappa_2, \kappa_3)$ to frequency Ω, in the absence of forcing, is

$$D(\Omega, \kappa_1, \kappa_2, \kappa_3) = \Omega^2 - 6 + 2(\cos\kappa_1 + \cos\kappa_2 + \cos\kappa_3) = 0, \quad (16)$$

the solution of which is plotted on figure 5(a) around the edges of the irreducible Brillouin zone which is represented in figure 5(b). The HFH asymptotic theory of [15] generates local asymptotic representations for the dispersion curves near the standing wave frequencies, which also act to validate the theory, and these are shown in figure 5(a) for completeness.

We consider the asymptotics of the well-known Fourier solution

$$y_{m,n,p} = \frac{1}{(2\pi)^3} \int_{-\pi}^{\pi}\int_{-\pi}^{\pi}\int_{-\pi}^{\pi} \frac{\exp[-i(k_1 m + k_2 n + k_3 p)]}{D(\Omega, k_1, k_2, k_3)} \mathrm{d}k_1 \mathrm{d}k_2 \mathrm{d}k_3 \quad (17)$$

using the scalings motivated by the two-dimensional square lattice. There are four points of interest on the boundary of the irreducible Brillouin zone R, X, M and I. The first three points lie at the vertices of the irreducible Brillouin zone and are standing waves in the conventional sense, while the fourth lies along the edge ΓM. The point Γ is not considered here as the long-wave low frequency asymptotics are straightforward.

3.1. Asymptotics near R

At point R of the irreducible Brillouin zone (see figure 5), the wavevector has coordinates (π, π, π) and the standing wave frequency is $\Omega_0^2 = 12$. We centre

the 2π-periodic triple integral (17) at that point and use the Ansatz (4). Since the stop band is delimited by Ω_0, we will get a propagating or exponentially decaying solution, depending on the sign of Ω_2^2. In the integral we make the change of variables $k_1 = \pi + \epsilon\alpha$, $k_2 = \pi + \epsilon\beta$, $k_3 = \pi + \epsilon\gamma$ and in the limit $\epsilon \to 0$

$$y_{m,n,p} = \frac{e^{-i\pi(m+n+p)}}{(2\pi)^3}\epsilon \int_{-\infty}^{\infty}\int_{-\infty}^{\infty}\int_{-\infty}^{\infty} \frac{\exp[-i(\alpha\eta_1 + \beta\eta_2 + \gamma\eta_3)]}{\alpha^2 + \beta^2 + \gamma^2 + \Omega_2^2} \mathrm{d}\alpha\mathrm{d}\beta\mathrm{d}\gamma + \mathcal{O}(\epsilon^2) \tag{18}$$

after introducing the long-scale variable $\boldsymbol{\eta} = (\eta_1, \eta_2, \eta_3) = \epsilon(m, n, p)$. The integral isolates an oscillatory short-scale $Y_{m,n,p} = \epsilon \exp[-i(m + n + p)\pi]$, and a long-scale component $f(\boldsymbol{\eta})$ as the remaining Fourier integral which is simply

$$f(\boldsymbol{\eta}) = \frac{\exp\left[i\sqrt{-\Omega_2^2}r\right]}{4\pi r}, \tag{19}$$

where $r = \sqrt{\eta_1^2 + \eta_2^2 + \eta_3^2}$. Hence if $\Omega_2^2 > 0$, the solution decays exponentially, and for $\Omega_2^2 < 0$, the wave propagates, in agreement with the dispersion curve. The propagation is isotropic and analogous to the two dimensional lattice at M; the concentric wavefronts of figure 2(a) become concentric spheres. Making use of the high frequency homogenisation of [15], together with the Ansätze

$$y_{m,n,p} = y_{0,m,n,p} + \epsilon y_{1,m,n,p} + \epsilon^2 y_{2,m,n,p} + \mathcal{O}(\epsilon^3),\ \Omega^2 = \Omega_0^2 + \epsilon\Omega_1^2 + \epsilon^2\Omega_2^2 + \mathcal{O}(\epsilon^3), \tag{20}$$

and the introduction of a source term $\delta_{0,0,0}/\epsilon$ on the right-hand side, the difference equation (15) generates the elliptic partial differential equation on the macroscale,

$$f_{\eta_1\eta_1}(\boldsymbol{\eta}) + f_{\eta_2\eta_2}(\boldsymbol{\eta}) + f_{\eta_3\eta_3}(\boldsymbol{\eta}) - \Omega_2^2 f(\boldsymbol{\eta}) = -\delta(\eta_1)\delta(\eta_2)\delta(\eta_3). \tag{21}$$

Equation (21) has the solution (19). It is worth noting that in three-dimensional structures, an $\mathcal{O}(1)$ source term yields a $\mathcal{O}(\epsilon)$ solution, hence the presence of the ϵ factor in $Y_{m,n,p}$. Throughout this whole section, we will use the source term $\delta_{0,0,0}/\epsilon$ when discussing high frequency homogenisation.

3.2. Asymptotics near X

At point X of the irreducible Brillouin zone (see figure 5), the wavevector has coordinates $(0, \pi, 0)$ and the standing wave frequency is $\Omega_0 = 2$. Using the Ansatz (4), and the change of variables $k_1 = \epsilon\alpha$, $k_2 = \pi + \epsilon\beta$, $k_3 = \epsilon\gamma$, in (17) gives

$$y_{m,n,p} = \frac{e^{-in\pi}}{(2\pi)^3}\epsilon \int_{-\infty}^{\infty}\int_{-\infty}^{\infty}\int_{-\infty}^{\infty} \frac{\exp[-i(\alpha\eta_1 + \beta\eta_2 + \gamma\eta_3)]}{-\alpha^2 + \beta^2 - \gamma^2 + \Omega_2^2} \mathrm{d}\alpha\mathrm{d}\beta\mathrm{d}\gamma + \mathcal{O}(\epsilon^2) \tag{22}$$

as $\epsilon \to 0$. The long-scale variable is $\boldsymbol{\eta} = (\eta_1, \eta_2, \eta_3) = \epsilon(m, n, p)$. This leads to a natural separation of scales with $Y_{m,n,p} = \epsilon \exp[-in\pi]$ and a long-scale function

$$f(\boldsymbol{\eta}) = \frac{\exp\left[i\sqrt{\Omega_2^2\rho^2}\right]}{4\pi\rho}, \tag{23}$$

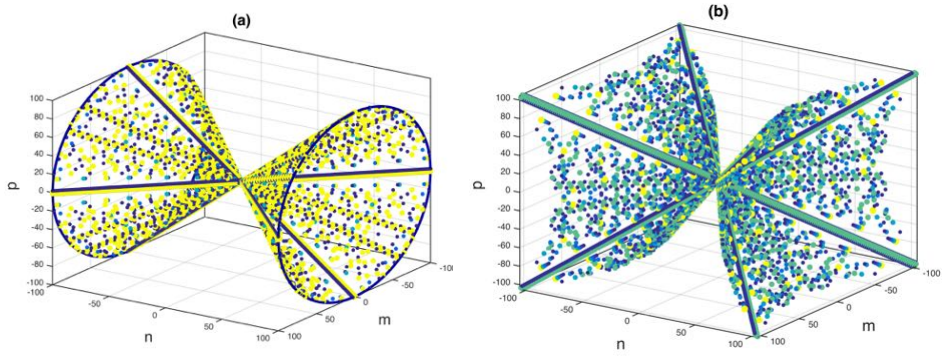

Figure 6: Macroscale asymptotic cone-shaped solutions from equation (23) on panel (a) (corresponding to point X or M) and from equation (38) on panel (b) (corresponding to point I).

where $\rho^2 = \eta_1^2 - \eta_2^2 + \eta_3^2$; this function is plotted on figure 6(a) and it is an infinite cone with axis parallel to the η_2-axis. It is worth noting that the solution is singular when $\rho = 0$, and that depending on the sign of $\Omega_2^2\rho^2$, the solution will either propagate ($\Omega_2^2\rho^2 > 0$) or exponentially decay ($\Omega_2^2\rho^2 < 0$). To see details of the short-scale behaviour, we examine a two-dimensional slice of the solution for positive and negative perturbations. For instance, in the plane $\eta_3 = 0$, the solution will be divided in pieces valid in the four quadrants separated by the line $\eta_1 = \pm\eta_2$ (see figure 7 panels (c),(d)). In each quadrant, the solution is the sum of propagating solutions, which dominate, and exponentially decaying solutions. This is analogous to the behaviour shown in two-dimensions in figures 3,4 and discussed in section 2(b). The cubic lattice Brillouin zone has three equivalent X points, $(0, \pi, 0)$, $(\pi, 0, 0)$ and $(0, 0, \pi)$, denoted as $\hat{X}$, X and $\tilde{X}$, respectively. We can perform the analysis around each point to get a cone on the long-scale and $\hat{Y}_{m,n,p} = \epsilon \exp[-im\pi]$ and $\hat{\rho}^2 = -\eta_1^2 + \eta_2^2 + \eta_3^2$ at $\hat{X}$ and $\tilde{Y}_{m,n,p} = \epsilon \exp[-ip\pi]$ and $\tilde{\rho}^2 = \eta_1^2 + \eta_2^2 - \eta_3^2$ at $\tilde{X}$. These two solutions also give infinite cones, one oriented along the η_1-axis for $\hat{X}$ and one oriented along the η_3-axis for $\tilde{X}$. The three cones, with orthogonal axes, then intersect along the characteristic lines $\eta_i = \pm\eta_j$, $\eta_k = 0$ for $(i, j, k) \in 1, 2, 3$, where (23) is singular.

The full solution close to the frequency $\Omega_0 = 2$ is the sum of those at $\hat{X}$, X and $\tilde{X}$. All the solutions give high dynamic anisotropy along the characteristic lines mentioned above. However, their contributions differ on the short-scale. For instance, in the plane $\eta_3 = 0$, the contribution from X (antiperiodicity along n-axis) dominates in quadrants 2 and 4 for $\Omega_2^2 > 0$ and in quadrants 1 and 3 for $\Omega_2^2 < 0$, and the contribution from $\hat{X}$ dominates in the complementary quadrants.

Applying the homogenisation theory [15] with Ansatz (20) a long-scale Klein-Gordon equation is deduced

$$f_{\eta_1\eta_1}(\boldsymbol{\eta}) - f_{\eta_2\eta_2}(\boldsymbol{\eta}) + f_{\eta_3\eta_3}(\boldsymbol{\eta}) + \Omega_2^2 f(\boldsymbol{\eta}) = \delta(\eta_1)\delta(\eta_2)\delta(\eta_3), \tag{24}$$

and (23) also follows.

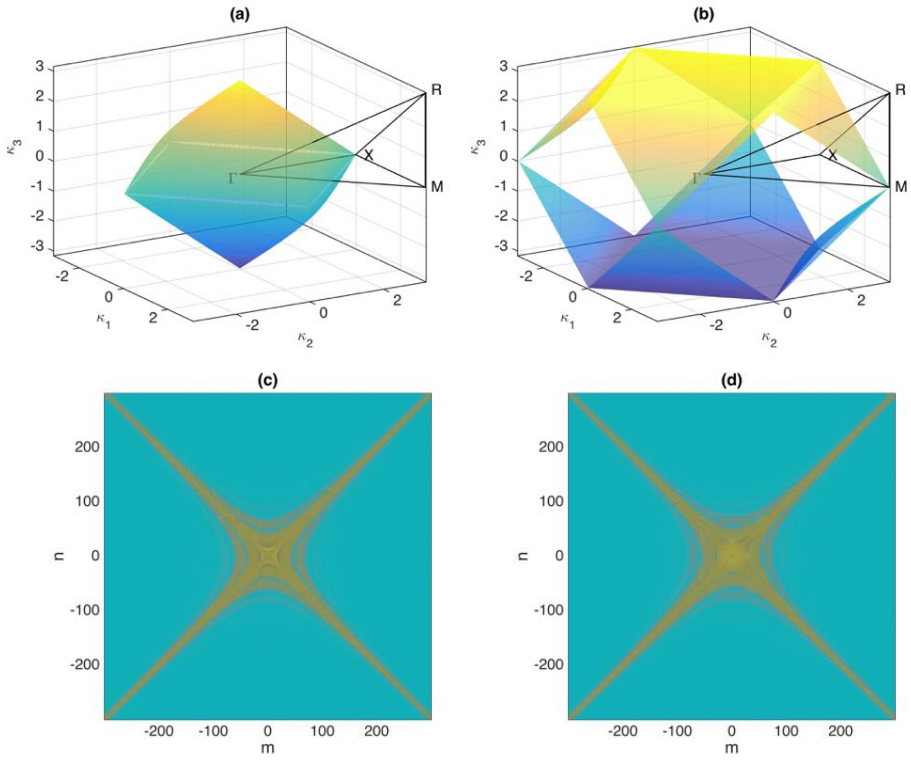

Figure 7: Panels (a) (resp. (b)) shows the isofrequency surface for $\Omega = 2$ (resp. $\Omega = \sqrt{8}$). Panels (c) and (d) are a slice in the $p = 0$ plane showing the microscale behaviour of the highly directional anisotropy for the cubic periodic lattice excited at the origin; numerically this has been done using the FFT. Panel (c) is for $\Omega_2^2 < 0$ and panel (d) is for $\Omega_2^2 > 0$.

The asymptotic results above are in agreement with the numerics on figure 7. In this section, the numerics were computed using the Fast Fourier Transform already implemented in Matlab. Panels (c) and (d) are slices in the plane $p = 0$ and resemble the two-dimensional crosses from figures 3,4, with a stronger damping but the main feature is the same, even on the microscale. Figure 8 on panel (a) shows the largest field values in three-dimensions and reveals the anisotropy with beams going from the origin along the characteristics, corresponding to the intersection of the three infinite cones.

3.3. Asymptotics near M

At point M of the irreducible Brillouin zone, (see figure 5), we choose the wavevector with coordinates $(\pi, 0, \pi)$ and the standing wave frequency is $\Omega_0 = \sqrt{8}$. We use the Ansatz (4) and make the change of variables $k_1 = \pi + \epsilon\alpha$,

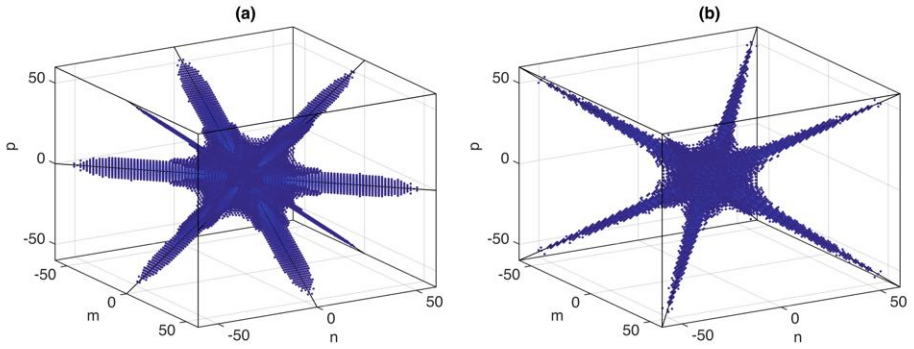

Figure 8: Highly directional anisotropy for the cubic periodic lattice excited at the origin, just below the standing wave frequency, at $\Omega = 2$ on panel (a), at $\Omega = \sqrt{6}$ on panel (b); numerically this has 241x241x241 masses surrounded with a 24 mass layer of PML. On the left panel, corresponding to points X,M the energy propagates along the characteristics of (23), on the right panel, corresponding to point I, the characteristics of (38).

$k_2 = \epsilon\beta$, $k_3 = \pi + \epsilon\gamma$ in the Fourier solution (17) in the limit $\epsilon \to 0$

$$y_{m,n,p} = \frac{e^{-i(m+p)\pi}}{(2\pi)^3}\epsilon \int_{-\infty}^{\infty}\int_{-\infty}^{\infty}\int_{-\infty}^{\infty} \frac{\exp[-i(\alpha\eta_1 + \beta\eta_2 + \gamma\eta_3)]}{\alpha^2 - \beta^2 + \gamma^2 + \Omega_2^2} \mathrm{d}\alpha\mathrm{d}\beta\mathrm{d}\gamma + \mathcal{O}(\epsilon^2) \tag{25}$$

with the long-scale variable $\boldsymbol{\eta} = (\eta_1, \eta_2, \eta_3) = \epsilon(m, n, p)$. The separation of scales yields $Y_{m,n,p} = \epsilon \exp[-i(m+p)\pi]$ and a long-scale function

$$f(\boldsymbol{\eta}) = \frac{\exp\left[i\sqrt{\Omega_2^2\rho^2}\right]}{4\pi\rho}, \tag{26}$$

where $\rho^2 = -\eta_1^2 + \eta_2^2 - \eta_3^2$.

Applying the high frequency homogenisation theory (see [15]) with the Ansatz (20), the following equation ensues for the envelope function

$$-f_{\eta_1\eta_1}(\boldsymbol{\eta}) + f_{\eta_2\eta_2}(\boldsymbol{\eta}) - f_{\eta_3\eta_3}(\boldsymbol{\eta}) + \Omega_2^2 f(\boldsymbol{\eta}) = \delta(\eta_1)\delta(\eta_2)\delta(\eta_3). \tag{27}$$

Multiplying this equation by -1, we recover (24) with a change of sign in front of the frequency and forcing terms. Hence, exciting above the standing wave frequency at X ($\Omega_0 = 2$ and $\Omega_2^2 > 0$) is equivalent to exciting below the standing wave frequency at M ($\Omega_0^2 = 8$ and $\Omega_2^2 < 0$), as long as the long-scale behaviour is concerned.

The above analysis regarding the highly anisotropic behaviour is complemented by looking at eigensolutions exactly at the standing wave frequencies. For the non-forced problem eigensolutions can be obtained at the points X and M by inspection as in [3] where, for the square lattice, they find $y_{n,m} = (-1)^n\delta_{\pm m,n}$ is a solution of the difference equation (1) exactly at frequency $\Omega = \Omega_0 = 2$.

It amounts to the whole lattice being at rest except along the diagonals $m = \pm n$, where neighbouring masses are out-of-phase. When forcing is present the asymptotics with the Hankel and Bessel functions account for the propagation or decay away from the forcing. For the cubic case, the difference equation without forcing (15) reduces to

$$y_{m+1,n,p}+y_{m-1,n,p}+y_{m,n+1,p}+y_{m,n-1,p}+y_{m,n,p+1}+y_{m,n,p-1}\pm 2y_{m,n,p} = 0 \quad (28)$$

for the frequencies $\Omega = \sqrt{8}$ (resp. $\Omega = 2$) for the positive sign (resp. negative sign). At these frequencies, the primitive solutions are

$$\begin{aligned} y_{m,n,p} &= (-1)^n \delta_{\pm m,n}, \quad \text{for} \quad \Omega = 2, \\ y_{m,n,p} &= (-1)^n (-1)^p \delta_{\pm m,n}, \quad \text{for} \quad \Omega = \sqrt{8}. \end{aligned} \quad (29)$$

From periodicity, the other X and M points give permutations in m, n, p of this solution. Using a cube of identical side centred at the origin as a reference, these solutions have the whole lattice at rest, except along the six lines going from the origin to the centre of each edge. With a forcing in the centre, there is propagation along the cones.

Thus far, points corresponding to standing wave frequencies (X,M,R) have been dealt with. These three points are special because they are vertices of the irreducible Brillouin zone (see figure 5(b)). It is often admitted in the literature [24] that when exciting lattices around those frequencies, the main contribution comes from the point in $\boldsymbol{\kappa}$-space situated on a vertex. The homogenisation is then straightforward since $\Omega_1^2 = 0$ and a second order partial differential equation ensues, giving the expected quadratic behaviour (see figure 5(a)).

3.4. Asymptotics near I

In this section we demonstrate the range of strongly directed modes that are missed when we restrict ourselves to solely traversing around the edges of the irreducible Brillouin zone. We shall broaden our asymptotic approach; whereby we now expand about a path in frequency-wavevector space, as opposed to pre-emptively constraining ourselves to a fixed point. For simplicity, we only examine the path $M\Gamma$ (shown in figure 5(a)) however the approach outlined herein, can be applied to any of the other edges. Finally, we will demonstrate that the strongest anisotropy occurs when the cubic lattice is excited in the vicinity of point I.

The wavevectors along the path $M\Gamma$ have the coordinates $(d, d, 0)$ where $d \in (0, \pi)$. Unlike the preceding sections, we do not fix d from the outset and we also no longer restrict ourselves to examining standing wave frequencies, hence the following expansion is taken

$$\Omega^2 \sim \Omega_0^2 + \epsilon\Omega_1^2 + \epsilon^2\Omega_2^2 \quad \text{where} \quad \Omega_0^2 = 4[1 - \cos(d)]. \quad (30)$$

As before, we shall utilise the well-known Fourier solution (17) and demonstrate its connection with high frequency homogenisation. Initially we apply the frequency expansion, along with the corresponding perturbation in wavevector space $k_1 = d + \epsilon\alpha, k_2 = d + \epsilon\beta, k_3 = \epsilon\gamma$ to the Fourier integral,

$$y_{m,n,p} = \epsilon^2 \frac{\epsilon^{-id(m+n)}}{(2\pi)^3} \int_{-\infty}^{\infty}\int_{-\infty}^{\infty}\int_{-\infty}^{\infty} \frac{\exp[-i(\alpha\eta_1 + \beta\eta_2 + \gamma\eta_3)]}{\Omega_1^2 - A_1(\boldsymbol{\alpha}; d) + \epsilon\left[\Omega_2^2 - A_2(\boldsymbol{\alpha}; d)\right]} \mathrm{d}\alpha\mathrm{d}\beta\mathrm{d}\gamma + \mathcal{O}(\epsilon^2),$$
$$A_1(\boldsymbol{\alpha}; d) = 2\sin(d)\left(\alpha + \beta\right), \quad A_2(\boldsymbol{\alpha}; d) = \cos(d)\left(\alpha^2 + \beta^2\right) + \gamma^2, \tag{31}$$

where $\boldsymbol{\alpha} = (\alpha, \beta, \gamma)$. We digress here and note that the Ω_1^2 term is proportional to the group velocity in the direction $\boldsymbol{\kappa}$. Therefore when we excite the lattice in the vicinity of a fixed point in frequency-wavevector space, Ω_0^2 (fixed d), the dominant modes of oscillations would be comprised of waves which satisfy the following condition

$$\Omega_1^2 = 2\Omega_0\left(\boldsymbol{\alpha}\cdot\nabla\Omega_0\right) = 2\Omega_0\sin(d)(\alpha + \beta) = 0, \tag{32}$$

where $\Omega_0 \neq 0$ along the path $M\Gamma$. It follows that this condition is satisfied when

$$\alpha = -\beta, \quad \gamma \in \mathbb{R}. \tag{33}$$

Therefore when we fix $d \in (0, \pi)$ the preceding equation defines an asymptotic plane to the point $(d, d, 0)$ in which the local group velocity is zero. The term $\Omega_1^2 - A_1$ vanishes and hence the remainder in (31) is $\mathcal{O}(\epsilon^2)$. Using condition (33) we can determine that the major contributing component of the integral (31) is

$$y_{m,n,p} = \epsilon \frac{e^{-id(m+n)}}{(2\pi)^3} \int_{-\infty}^{\infty}\int_{-\infty}^{\infty}\int_{-\infty}^{\infty} \frac{\exp[-i(\alpha\eta_1 + \beta\eta_2 + \gamma\eta_3)]}{\Omega_2^2 - \cos(d)\left(\alpha^2 + \beta^2\right) - \gamma^2} \mathrm{d}\alpha\mathrm{d}\beta\mathrm{d}\gamma + \mathcal{O}(\epsilon^2), \tag{34}$$

where the integrals are resolved explicitly to yield the following solution,

$$Y_{m,n,p} f(\boldsymbol{\eta}) = \epsilon \frac{\exp(i[d(m+n) + \sqrt{\Omega_2^2\rho^2}])}{4\pi\rho}$$
$$\text{where} \quad \rho^2 = \cos(d)\left(\eta_1^2 + \eta_2^2\right) + \eta_3^2. \tag{35}$$

From equation (35) we ascertain that there exists strongly directional oscillations if the lattice is excited in the vicinity of $\Omega_0^2 = 4[1 - \cos(d)]$ for fixed $d \in (\pi/2, \pi)$. We have shown previously how the Green's function approach and high frequency homogenisation technique are connected through the denominator of the lattice Green's function and the effective equation obtained by the latter. We have seen that hyperbolic equations are associated to anisotropic behaviour, which will be the case for $\cos(d) < 0$, and that the directional propagation is then along the characteristics of the effective equation. The value

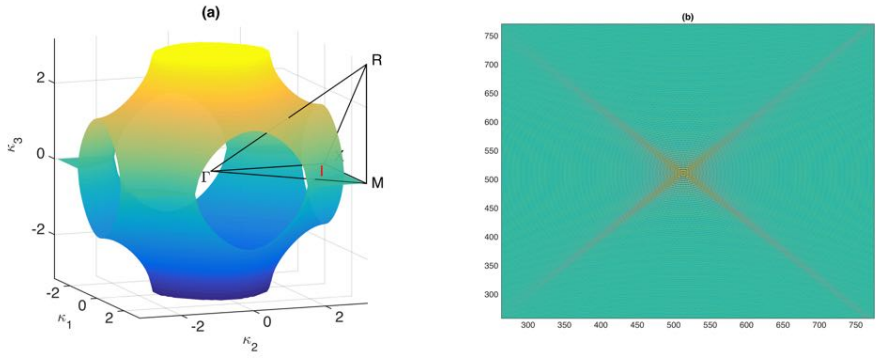

Figure 9: Isofrequency surface at $\Omega = \sqrt{6}$ on panel (a) and slice in the plane $m = n$ showing highly directional anisotropy in discrete mass-spring cubic periodic lattice excited at the origin for $d = 2\pi/3$ (at frequency $\Omega = \sqrt{6}$) on panel (b), numerically obtained using the FFT.

of d determines the sharpness of the behaviour. The most pronounced pattern is found when $\cos(d) = -1/2$; hence we define point I for wavevector $(2\pi/3, 2\pi/3, 0)$. The solution (35) is again a cone on the long-scale, it is shown in figure 6(b). The whole numerical solution is shown in figure 8(b). The energy propagates along the characteristics . Figure 9 shows a two-dimensional slice in the plane $m = n$.

We can perform a comparable analysis using high frequency homogenisation ([15]) whereby we introduce the source term, $\delta_{0,0,0}/\epsilon$ on the right-hand side of the difference equation (15). At leading order we obtain the frequency shown in equation (30) whilst at first-order we obtain the following partial differential equation,

$$2i\sin(d)\left[f_{\eta_1}(\boldsymbol{\eta}) + f_{\eta_2}(\boldsymbol{\eta})\right] + \Omega_1^2 f(\boldsymbol{\eta}) = 0. \tag{36}$$

Fourier transforming this equation and imposing condition (32) gives us the equation of the asymptotic plane, (33), in which the group velocity is zero. Proceeding to second-order, with this constraint imposed, we obtain the following,

$$\cos(d)\left[f_{\eta_1\eta_1}(\boldsymbol{\eta}) + f_{\eta_2\eta_2}(\boldsymbol{\eta})\right] + f_{\eta_3\eta_3}(\boldsymbol{\eta}) + \Omega_2^2 f(\boldsymbol{\eta}) = \delta(\eta_1)\,\delta(\eta_2)\,\delta(\eta_3)\,. \tag{37}$$

After some algebra, we find the following solution,

$$f(\boldsymbol{\eta}) = \frac{\exp\left(i\sqrt{\Omega_2^2\rho^2}\right)}{4\pi\rho}, \tag{38}$$

where ρ was previously defined in equation (35). By contrasting equation (35) with (38) we immediately retrieve the short-scale displacement term, $Y_{m,n,p} = \epsilon\exp\left[id(m+n)\right]$.

4. Elastic frames: An example

In the previous sections, an asymptotic method has been developed to study the properties of scalar lattice Green's functions in the vicinity of resonances in both two and three dimensions. In both cases a compact exact expression for the Green's functions exists in terms of Fourier integrals which allow the asymptotic method to be verified relatively easily.

Here, we consider the problem of a three-dimensional cubic lattice consisting of thin elastic ligaments. This problem can be seen as the natural generalisation of the two-dimensional problem considered in section 2, which corresponds to the out-of-plane deformation of a planar square array of masses connected by massless springs and has only one degree of freedom. The present problem is significantly more challenging for several reasons. A three-dimensional cubic lattice of thin elastic ligaments is a so-called "bending dominated" structure [16], which means that it is necessary to account for the flexural deformations of the lattice links in order to maintain stability. Therefore each lattice junction has six degrees of freedom (compared with one for the previous problems): three translation degrees of freedom and three rotational degrees of freedom. Each lattice link has three fundamental modes of deformation: compression and extension, flexion, and torsion. The six degrees of freedom results in a Green's tensor rather than Green's function, and makes the formal manipulations very cumbersome. Even the direct numerical approach of inverting the Fourier transform is a significant computational challenge as the inversion must be performed six times at each lattice site. Moreover, the dispersion equation is a sixth order polynomial in Ω^2 to which no closed form solutions exist in the general case. This serves to underline the power of the asymptotic approach developed herein: it is not necessary to explicitly formulate the Green's tensor or solve the dispersion equation directly.

4.1. Problem set-up

For the previous two cases considered, those of the square (§2) and cubic (§3) lattices, the Green's functions are oft-studied and well known. In contrast, the elastic Green's tensor for a three-dimensional cubic lattice of massless Euler-Bernoulli beams has received little attention. In the present section, and before developing the high-frequency homogenisation algorithm, we construct the Green's tensor for a cubic lattice of thin elastic ligaments.

Consider a slender massless Euler-Bernoulli beam of unit length oriented along the x_1-axis. The displacement field $\boldsymbol{y}(x_1) = [y_1(x_1), y_2(x_1), y_3(x_1)]^{\mathrm{T}}$ together with the rotations $\boldsymbol{\theta}(x_1) = [\theta_1(x_1), \theta_2(x_1), \theta_3(x_1)]^{\mathrm{T}}$ satisfy the following

boundary value problems (see [18] and [34], among others)

$$\frac{d^2y_1}{dx_1^2} = 0, \qquad y_1(0) = Y_1^{(0)}, \qquad y_1(1) = Y_1^{(1)}, \tag{39}$$

$$\frac{d^2\theta_1}{dx_1^2} = 0, \qquad \theta_1(0) = \Theta_1^{(0)}, \qquad \theta_1(1) = \Theta_1^{(1)}, \tag{40}$$

$$\frac{d^4y_i}{dx_1^4} = 0, \qquad y_i(0) = Y_i^{(0)}, \qquad y_i(1) = Y_i^{(1)}, \tag{41}$$

$$\frac{dy_i}{dx_1}(0) = (-1)^i\Theta_{5-i}^{(0)}, \qquad \frac{dy_i}{dx_1}(1) = (-1)^i\Theta_{5-i}^{(1)},$$

where Θ_i represents the counter-clockwise rotation about the x_i axis for $i = 2, 3$.

It is convenient to introduce the following non-dimensional parameters $a = K/(SE\ell^2)$ and $b = 2I/(S\ell^2)$, where K, S, I, E, and ℓ is the torsional rigidity, cross-sectional area, area moment of inertia, Young's modulus, and length of the beam respectively (see, [34] for further details). Physically, a and b can be associated with the ratio of torsional and flexural stiffness to compressional stiffness respectively. With this normalisation in place, the forces and moments exerted at $x_1 = 0$ are

$$F_1 = \frac{dy_1}{dx_1} \qquad F_2 = \frac{-b}{2}\frac{d^3y_2}{dx_1^3} \qquad F_3 = \frac{-b}{2}\frac{d^3y_3}{dx_1^3}$$
$$M_1 = a\frac{d\theta_1}{dx_1} \qquad M_2 = \frac{-b}{2}\frac{d^3y_3}{dx_1^3}\bigg|_{x_1=0} \qquad M_3 = \frac{-b}{2}\frac{d^3y_2}{dx_1^3}\bigg|_{x_1=0},$$

whence the equilibrium equation at $x_1 = 0$ may be written.

$$\boldsymbol{F} = A\boldsymbol{Y}^{(0)} + B\boldsymbol{Y}^{(1)} \tag{42}$$

where $\boldsymbol{F} = [F_1, F_2, F_3, M_1, M_2, M_3]^{\mathrm{T}}$ and $\boldsymbol{Y}^{(j)} = [Y_1^{(j)}, Y_2^{(j)}, Y_3^{(j)}, \Theta_1^{(j)}, \Theta_2^{(j)}, \Theta_3^{(j)}]^{\mathrm{T}}$ are the forcing and displacement vectors for $j = 0, 1$. The matrices A and B are the sparse 6×6 stiffness matrices linking the displacements at the ends of the beam to the force at $x_1 = 0$ and are provided in appendix A.

Having established the equilibrium equation for a beam oriented along the x_1-axis, the corresponding equation for a beam oriented along any of the five remaining directions can be obtained by mapping the displacements onto the x_1-axis and the resulting forces back into global coordinates. In this way we can construct the equilibrium equation for any point in the lattice. To this end we introduce the unitary rotation matrices R_{ij} (see appendix A) which map the i^{th} axis to the j^{th}; R_{ii} maps $x_i \mapsto -x_i$. Imposing the Bloch-Floquet quasi periodicity condition then yields the equations of motion for time-harmonic waves of the form $-\mathcal{M}\Omega^2\boldsymbol{y}_{m,n,p} = \sigma\boldsymbol{y}_{m,n,p}$ with

$$\begin{aligned}\sigma = {} & A + R_{12}AR_{12}^T + R_{11}AR_{11}^T + R_{21}AR_{21}^T \\ & + R_{13}AR_{13}^T + R_{31}AR_{31}^T + Be^{ik_1} + R_{12}BR_{21}^Te^{ik_2} + R_{11}BR_{11}^Te^{-ik_1} \\ & + R_{21}BR_{21}^Te^{-ik_2} + R_{13}BR_{31}^Te^{ik_3} + R_{31}BR_{31}^Te^{-ik_3},\end{aligned} \tag{43}$$

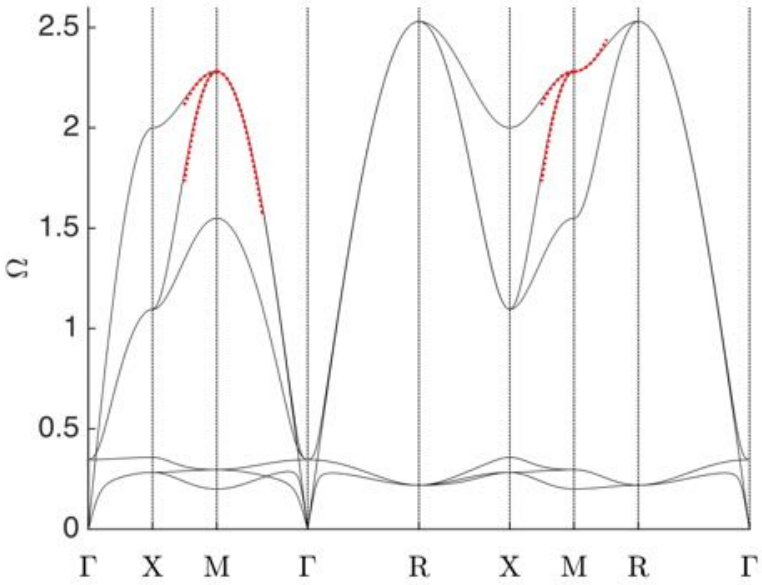

Figure 10: Dispersion curves around the edges of the Brillouin zone for parameters $a = 0.01$ (torsional rigidity of the rods), $b = 0.05$ (flexural rigidity of the rods), $J = 5$ (polar moment of inertia of the links). The solid curves show solutions of the full dispersion equation, whereas the dashed red curves indicate the asymptotic expansions.

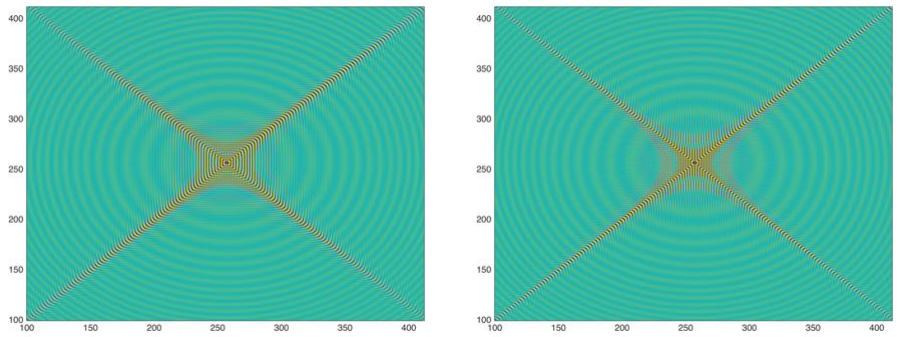

Figure 11: An example of the highly anisotropic dynamic response for a 3D elastic lattice when forced at a single point. The two panels show the first component of the displacement field over a cross-section in the plane $m = 0$ through the origin. The numerical parameters are taken as $a = 0.01$, $b = 0.05$, $J = 5$, at frequency $\Omega = \sqrt{\Omega_0^2 - 0.01}$ on the left panel and $\sqrt{\Omega_0^2 + 0.01}$ on the right panel with $\Omega_0^2 = 24b + 4$.

$\mathcal{M} = \mathrm{diag}(1, 1, 1, J, J, J)$ and J is the non-dimensionalised polar mass moment of inertia. The dispersion relation is then

$$\det\left(\sigma + \Omega^2 \mathcal{M}\right) = 0,$$

with the irreducible Brillouin zone being the same as the cubic scalar case (figure 5). We plot the dispersion relation around the edges of the irreducible Brillouin zone. If we apply a force at the origin of the system, i.e. at $(m, n, p) = \mathbf{0}$, the Green's tensor is

$$\boldsymbol{y}_{m,n,p} = \frac{1}{(2\pi)^3} \int_{-\pi}^{\pi}\int_{-\pi}^{\pi}\int_{-\pi}^{\pi} (\sigma + \Omega^2 \mathcal{M})^{-1} \cdot \boldsymbol{F} e^{-i(mk_1 + nk_2 + pk_3)} \mathrm{d}k_1 \mathrm{d}k_2 \mathrm{d}k_3. \quad (44)$$

The components of the Green's tensor $\boldsymbol{y}_{m,n,p}$ and matrix σ are not stated explicitly here in the interests of brevity.

4.2. Homogenisation

For definiteness we consider the asymptotic expansion of the Green's tensor (44) about the point M in the Brillouin zone, that is, for wave vector $(\kappa_1, \kappa_2, \kappa_3) = (\pi, \pi, 0)$. At this point the highest two branches of the dispersion curves, shown in figure 10, exhibit the characteristic changes in curvature associated with strong anisotropic wave propagation. This effect has been analysed in the preceding sections for the two- and three-dimensional scalar lattices.

We will follow broadly the same approach employed in earlier sections. However, in order to avoid the tedious manipulations associated with operating directly on the Green's tensor itself, we begin by considering the forced problem

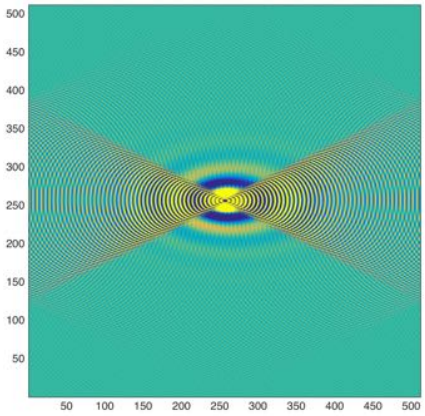

Figure 12: The same configuration as in figure 11, except that here we show the first component of the displacement field over the plane $p = 0$. The forcing frequency is chosen as $\Omega = \sqrt{\Omega_0^2 - 0.01}$ with $\Omega_0^2 = 24b + 4$.

in Fourier space. In particular, the lattice Green's tensor satisfies the inhomogeneous vector problem

$$\left[\sigma(k_1, k_2, k_3) + \Omega^2 \mathcal{M}\right] \boldsymbol{y}^{\mathrm{F}} = \boldsymbol{F}, \tag{45}$$

were $\boldsymbol{F} = (F_1, F_2, F_3, F_4, F_5, F_6)$ is some forcing vector. In contrast to the previously considered scalar cases, we have some freedom in how we choose to apply the forcing. Physically, each component of $\boldsymbol{F}$ corresponds to a different orientation of the applied load. We can choose to apply a point force directed along any linear combination of coordinate axis. We can also choose to apply point torques about any of the three principle axes; for now, we leave $\boldsymbol{F}$ arbitrary.

In parallel with earlier sections, we wish to express the Green's tensor as a product between the short-scale oscillatory component $Y_{m,n,p}$ and a long-scale contribution. In the cases considered thus far, the short-scale oscillatory function is simply the eigensolution of the homogeneous problem. Although we follow the same approach here, it is important to note that the homogeneous problem is degenerate at M, as indicated by the intersection of the highest two branches in figure 10. Hence, the general solution is a linear combination of the two linearly independent solutions [11] and we search for solutions of the Fourier transformed problem in the form $\boldsymbol{y}^{\mathrm{F}} = Y_{m,n,p}[\boldsymbol{Y}_1^{\mathrm{F}} y_1(\boldsymbol{\eta}) + \boldsymbol{Y}_2^{\mathrm{F}} y_2(\boldsymbol{\eta})]$, where $\boldsymbol{\eta} = \epsilon(m, n, p)$ is the usual long-scale variable and $\boldsymbol{Y}_j^{\mathrm{F}}$ satisfy $\left[\sigma(\pi, \pi, 0) + \Omega^2 \mathcal{M}\right] \boldsymbol{Y}_j^{\mathrm{F}} = 0$ for $j = 1, 2$. In particular, at M, we have $\boldsymbol{Y}_1^{\mathrm{F}} = [1, 0, 0, 0, 0, 0]^{\mathrm{T}}$ and $\boldsymbol{Y}_2^{\mathrm{F}} = [0, 1, 0, 0, 0, 0]^{\mathrm{T}}$. We make the change of variables $\boldsymbol{k} = (\pi + \epsilon\alpha, \pi + \epsilon\beta, \epsilon\gamma)$, for $0 < \epsilon \ll 1$ and expand $\Omega^2 \sim \Omega_0^2 + \epsilon\Omega_1^2 + \epsilon^2\Omega_2^2$ where $\Omega_0^2 = 24b + 4$ is the degenerate eigenvalue of $\left[\sigma(\pi, \pi, 0) + \Omega_0^2 \mathcal{M}\right] \boldsymbol{Y}_j^{\mathrm{F}} = 0$ corresponding to the two modes of interest. In this case, the forced problem

becomes

$$\left[\epsilon\left[\sigma_1(\alpha,\beta,\gamma)+\Omega_1^2\mathcal{M}\right]+\epsilon^2\left[\sigma_2(\alpha,\beta,\gamma)+\Omega_2^2\mathcal{M}\right]+\mathcal{O}(\epsilon^3)\right]\boldsymbol{y}_{m,n,p}=\boldsymbol{F}, \quad (46)$$

where the matrices σ_1 and σ_2 are given in appendix A. We now proceed by premultiplying (46) by one of the eigenvectors of the homogeneous problem. Using the fact that $\left(\boldsymbol{Y}_i^{\mathrm{F}}\right)^{\mathrm{T}}\sigma_1(\alpha,\beta,\gamma)\boldsymbol{Y}_j^{\mathrm{F}}=0$, we deduce that $\Omega_1=0$ and are left with

$$\epsilon^2\left(\boldsymbol{Y}_i^{\mathrm{F}}\right)^{\mathrm{T}}\left[\sigma_2(\alpha,\beta,\gamma)+\Omega_2^2\mathcal{M}\right]\boldsymbol{y}^{\mathrm{F}}=\boldsymbol{Y}_i^{\mathrm{F}}\cdot\boldsymbol{F}. \quad (47)$$

Equation (47) represents a pair of uncoupled algebraic equations for the long-scale envelope functions. Inversion the Fourier transforms leads to

$$y_1(\boldsymbol{\eta})=\epsilon\frac{F_1}{(2\pi)^3}\int_{-\infty}^{\infty}\int_{-\infty}^{\infty}\int_{-\infty}^{\infty}\frac{\exp[-i(\alpha\eta_1+\beta\eta_2+\gamma\eta_3)]}{\alpha^2+6b\beta^2-6b\gamma^2+\Omega_2^2}\mathrm{d}\alpha\mathrm{d}\beta\mathrm{d}\gamma+\mathcal{O}(\epsilon^2), \quad (48a)$$

$$y_2(\boldsymbol{\eta})=\epsilon\frac{F_2}{(2\pi)^3}\int_{-\infty}^{\infty}\int_{-\infty}^{\infty}\int_{-\infty}^{\infty}\frac{\exp[-i(\alpha\eta_1+\beta\eta_2+\gamma\eta_3)]}{6b\alpha^2+\beta^2-6b\gamma^2+\Omega_2^2}\mathrm{d}\alpha\mathrm{d}\beta\mathrm{d}\gamma+\mathcal{O}(\epsilon^2), \quad (48b)$$

where we have already factored out the short-scale oscillatory part $Y_{m,n,p}=\exp\left[-i(m+n)\right]$. The integrals (48) can again be evaluated explicitly to yield the long-scale envelope functions of similar form to those obtained for the cubic scalar lattice

$$y_j(\boldsymbol{\eta})=\epsilon F_j\frac{\exp\left(i\sqrt{\Omega_2^2\rho_j^2}\right)}{4\pi\rho_j}, \quad \text{for} \quad j=1,2, \quad (49)$$

with $\rho_1^2=\eta_1^2+6b\eta_2^2-6b\eta_3^2$ and $\rho_2^2=6b\eta_1^2+\eta_2^2-6b\eta_3^2$.

Equations (49) describe the long-scale behaviour of the lattice of near the resonant frequency $\Omega_0^2=24b+4$. It is immediately apparent from equations (48) and (49) that we can isolate each mode on the long-scale by choosing an appropriate forcing. Although we now deal with a very different physical problem, there is a remarkable similarity between the long-scale response of the present mechanical lattice and the much simpler lattice systems considered earlier. The overall structure of the components of the homogenised Green's tensor (48) is identical to the Green's functions considered earlier. This serves to demonstrate the power and universal applicability of the homogenisation method developed herein.

As in the earlier cases, the asymptotic expansion of the dispersion equation in the neighbourhood of point M appears as the denominator of the integrand of (48). These asymptotic expansions are shown as the dashed curves in figure 10.

Each long-scale solution (49) $y_i(\boldsymbol{\eta})$ is singular on the cones defined by $\rho_j=0$. Away from these cones, the long-scale solution will correspond to either a propagating or evanescent wave, depending on the sign of $\Omega_2^2\rho_j^2$. As for the two- and three-dimensional scalar problems considered in §2(2.2) & 3(3.2), this behavior is associated with highly localised star-shaped waveforms. Figures 11 & 12

show the first component of the displacement field associated with the Green's tensor for a forcing vector $\boldsymbol{F} = [1, 0, 0, 0, 0, 0]^{\mathrm{T}}$. The remaining components of the Green's tensor are vanishingly small in this configuration. The two panels of figure 11 show the field over the plane $m = 0$, with the cross-shapes clearly visible. The second figure 12 shows the field over the cross-section $p = 0$. Again the asymptotics conveniently capture the salient details of the lattice's behaviour, with the energy being directed along the characteristic cones of (49).

5. Concluding remarks

Here we demonstrate that one can connect homogenisation techniques based around two-scale expansions with the lattice Green's function approach for lattice dynamics. The methodology works well even when the explicit form of the Green function is disguised by matrix algebra, as in the frames example of section 4. Both approaches, the Greens function and homogenisation have their relative advantages but it is worth noting that the latter is easily extended to situations in continuum mechanics where no explicit Green's function is available or where the medium is no longer perfectly periodic.

Through the examples considered here we demonstrate that, although the physical configurations are very different, the lattice Green's function expansion approach not only remains valid, but also highlights the connection between the Green's functions for different systems. Indeed the overall form as well as the macroscopic response of the systems considered here are remarkably similar further demonstrating the power of the approach developed in the present paper.

In physical terms it is notable that the strong dynamic anisotropy observed for two-dimensional structures is clearly generalisable to three-dimensions; the cubic lattice that we treat contains the exemplar cases with strongly localised motion along beams readily identified from the asymptotic analysis. This should, as in the two-dimensional case [8], motivate experimental studies and motivate studies of the analogous examples in three-dimensional continuum systems.

Due to the computational cost of studying three-dimensional lattices numerically, particularly for continuous systems as three-dimensional lattices in Maxwell's equations or in elasticity, many, if not most, computations are in two-dimensions. Even for lattices, as here, performing the FFT for three-dimensional lattices is computationally very expensive, even for the rather simple scalar discrete problem. In order to reduce the simulation time to a practical length, we made full use of the parallelised FFT code available and employed a machine with 22 cores and 256GB of RAM. The ease by which the high frequency homogenisation pares the problem down to its bare essentials, and its accuracy, highlight its potential in more complicated systems.

Acknowledgements

RVC thanks the EPSRC (UK) for their support through research grants EP/L024926/1 & EP/J009636/1. The authors thank Younes Achaoui, Sebastien Guenneau and Alexander Movchan for helpful conversations.

References

[1] Abramowitz, M. & Stegun, I. A. 1964 *Handbook of Mathematical Functions*. Washington: National Bureau of Standards.

[2] Antonakakis, T., Craster, R. V. & Guenneau, S. 2013 Asymptotics for metamaterials and photonic crystals. *Proc. R. Soc. Lond.* A **469**, 20120533.

[3] Ayzenberg-Stepanenko, M. V. & Slepyan, L. I. 2008 Resonant-frequency primitive waveforms and star waves in lattices. *J. Sound Vib.* **313**, 812–821.

[4] Bensoussan, A., Lions, J.L. & Papanicolaou, G. 1978 *Asymptotic analysis for periodic structures*. North-Holland, Amsterdam.

[5] Birman, M. Sh. & Suslina, T. A. 2006 Homogenization of a multidimensional periodic elliptic operator in a neighborhood of the edge of an internal gap. *Journal of Mathematical Sciences* **136**, 3682–3690.

[6] Born, M. & Huang, K. 1954 *Dynamical theory of crystal lattices*. Oxford: Clarendon Press.

[7] Brillouin, L. 1953 *Wave propagation in periodic structures: electric filters and crystal lattices*, 2nd edn. New York: Dover.

[8] Ceresoli, L., Abdeddaim, R., Antonakakis, T., Maling, B., Chmiaa, M., Sabouroux, P., Tayeb, G., Enoch, S., Craster, R. V. & Guenneau, S. 2015 Dynamic effective anisotropy: Asymptotics, simulations and microwave experiments with dielectric fibres. *Phys. Rev. B* **92**, 174307.

[9] Chigrin, D. N., Enoch, S., Torres, C. M. S. & Tayeb, G. 2003 Self-guiding in two-dimensional photonic crystals. *Optics Express* **11**, 1203–1211.

[10] Chow, P.-L. 1973 Wave propagation in a random lattice II. *J. Math. Phys.* **14**, 1364–1373.

[11] Colquitt, D. J., Craster, R. V. & Makwana, M. 2015 High frequency homogenisation for elastic lattices. *The Quarterly Journal of Mechanics and Applied Mathematics* **68** (2), 203–230.

[12] Colquitt, D. J., Jones, I. S., Movchan, N. V., Movchan, A. B. & McPhedran, R. C. 2012 Dynamic anisotropy and localization in elastic lattice systems. *Waves Random Complex Media* **22**, 143–159.

[13] Colquitt, D. J., Nieves, M. J., Jones, I. S., Movchan, A. B. & Movchan, N. V. 2013 Localisation for a line defect in an infinite square lattice. *Proc. R. Soc. Lond.* A **469**, 20120579.

[14] Craster, R. V., Antonakakis, T., Makwana, M. & Guenneau, S. 2012 Dangers of using the edges of the Brillouin zone. *Phys. Rev. B* **86**, 115130.

[15] Craster, R. V., Kaplunov, J. & Postnova, J. 2010 High frequency asymptotics, homogenization and localization for lattices. *Q. Jl. Mech. Appl. Math.* **63**, 497–519.

[16] Deshpande, V. S., Ashby, M. F. & Fleck, N. A. 2001 Foam topology bending versus stretching dominated architectures. *Acta Materiala* **49**, 1035–1040.

[17] Economou, E. N. 1983 *Green's functions in quantum mechanics*. Berlin: Springer Verlag.

[18] Graff, K. F. 1975 *Wave motion in elastic solids*. Oxford University Press.

[19] Kittel, C. 1996 *Introduction to solid state physics*, 7th edn. New York: John Wiley & Sons.

[20] Koster, G. F. 1954 Theory of scattering in solids. *Phys. Rev.* pp. 1436–1443.

[21] Kutsenko, A. A. 2015 Explicit formula for amplitudes of waves in lattices with defects and sources and its application for defects detection. *Euro. J. Mech A/ Solids* **54**, 209–217.

[22] Langley, R. S. 1997 The response of two-dimensional periodic structures to point harmonic forcing. *J. Sound Vib.* **197**, 447–469.

[23] Lifshitz, I. M. & Kosevich, A. M. 1966 The dynamics of a crystal lattice with defects. *Rep. Prog. Phys.* **29**, 217–254.

[24] Lourtioz, J.-M., Benisty, H., Berger, V., Gerard, J.-M., Maystre, D. & Tchelnokov, A. 2008 *Photonic crystals: Towards Nanoscale Photonic Devices*. Springer.

[25] Makwana, M. & Craster, R. V. 2013 Localized defect states for high frequency homogenized lattice models. *Quart. J. Mech. Appl. Math.* **66**, 289–316, doi:10.1093/qjmam/hbt005.

[26] Maradudin, A. A. 1965 Some effects of point defects on the vibrations of crystal lattices. *Rep. Prog. Phys.* **28**, 332–380.

[27] Maradudin, A. A., Montroll, E. W., Weiss, G. H. & Ipatova, I. P. 1971 *Theory of Lattice dynamics in the harmonic approximation*. New York: Academic Press.

[28] Martin, P. A. 2006 Discrete scattering theory: Green's function for a square lattice. *Wave Motion* **43**, 619–629.

[29] Movchan, A. B. & Slepyan, L. I. 2007 Band gap Green functions and localised oscillations. *Proc. R. Soc. Lond.* A **463**, 2709–2727.

[30] Movchan, A. B. & Slepyan, L. I. 2014 Resonant waves in elastic structured media: Dynamic homogenisation versus green's functions. *Int. J. Solids Struct.* **51**, 2254–2260.

[31] Osharovich, G., Ayzenberg-Stepanenko, M. & Tsareva, O. 2010 Wave propagation in elastic lattices subjected to a local harmonic loading. II. Two dimensional problems. *Continuum Mech. Thermodyn.* **22**, 599–616.

[32] Osharovich, G. G. & Ayzenberg-Stepanenko, M. V. 2012 Wave localization in stratified square-cell lattices: The antiplane problem. *J. Sound Vib.* **331**, 1378–1397.

[33] Ostoja-Starzewski, M. 2002 Lattice models in micromechanics. *Appl. Mech. Rev.* **55**, 35–60.

[34] Timoshenko, S.P. & Goodier, J.N. 1951 *Theory of elasticity*, 3rd edn. New York: McGraw-Hill.

[35] Zucker, I. J. 2011 70+ years of the Watson integrals. *J. Stat. Phys.* **145**, 591–612.

A. Stiffness and rotation matrices

The stiffness matrices as used in equation (42) can be derived from the solution of the boundary value problems (39)–(41).

$$A = \begin{pmatrix} -1 & 0 & 0 & 0 & 0 & 0 \\ 0 & -6b & 0 & 0 & 0 & -3b \\ 0 & 0 & -6b & 0 & 3b & 0 \\ 0 & 0 & 0 & -a & 0 & 0 \\ 0 & 0 & 3b & 0 & -2b & 0 \\ 0 & -3b & 0 & 0 & 0 & -2b \end{pmatrix}, B = \begin{pmatrix} 1 & 0 & 0 & 0 & 0 & 0 \\ 0 & 6b & 0 & 0 & 0 & -3b \\ 0 & 0 & 6b & 0 & 3b & 0 \\ 0 & 0 & 0 & a & 0 & 0 \\ 0 & 0 & -3b & 0 & -b & 0 \\ 0 & 3b & 0 & 0 & 0 & -b \end{pmatrix}.$$

We now define the unitary rotation matrices R_{ij} that map the x_i-axis to the x_j-axis as follows

$$R_{11} = \begin{pmatrix} -1 & 0 & 0 & 0 & 0 & 0 \\ 0 & -1 & 0 & 0 & 0 & 0 \\ 0 & 0 & 1 & 0 & 0 & 0 \\ 0 & 0 & 0 & -1 & 0 & 0 \\ 0 & 0 & 0 & 0 & -1 & 0 \\ 0 & 0 & 0 & 0 & 0 & 1 \end{pmatrix}, \tag{50}$$

$$R_{12} = \begin{pmatrix} 0 & -1 & 0 & 0 & 0 & 0 \\ 1 & 0 & 0 & 0 & 0 & 0 \\ 0 & 0 & 1 & 0 & 0 & 0 \\ 0 & 0 & 0 & 0 & -1 & 0 \\ 0 & 0 & 0 & 1 & 0 & 0 \\ 0 & 0 & 0 & 0 & 0 & 1 \end{pmatrix}, \quad R_{13} = \begin{pmatrix} 0 & 0 & -1 & 0 & 0 & 0 \\ 0 & 1 & 0 & 0 & 0 & 0 \\ 1 & 0 & 0 & 0 & 0 & 0 \\ 0 & 0 & 0 & 0 & 0 & -1 \\ 0 & 0 & 0 & 0 & 1 & 0 \\ 0 & 0 & 0 & 1 & 0 & 0 \end{pmatrix}.$$

We have $R_{21} = R_{12}^T$ and $R_{31} = R_{13}^T$.

The matrices σ_1 and σ_2 have the form

$$\sigma_1 = \begin{pmatrix} 0 & 0 & 0 & 0 & -6ib\gamma & -6ib\beta \\ 0 & 0 & 0 & 6ib\gamma & 0 & 6ib\alpha \\ 0 & 0 & 0 & 6ib\beta & -6ib\alpha & 0 \\ 0 & -6ib\gamma & -6ib\beta & 0 & 0 & 0 \\ 6ib\gamma & 0 & 6ib\alpha & 0 & 0 & 0 \\ 6ib\beta & -6ib\alpha & 0 & 0 & 0 & 0 \end{pmatrix} \tag{51}$$

and

$$\begin{aligned} \sigma_2 = \mathrm{diag}[&\alpha^2 + 6b\beta^2 - 6b\gamma^2, \alpha^2 + 6b\beta^2 - 6b\gamma^2, 4(1-6b) + 6\alpha^2 + 6b\beta^2 - \gamma^2, \\ &4J(1+6b) - 4(a+2b) + a\alpha^2 - b\beta^2 + b\gamma^2, \\ &4J(1+6b) - 4(a+2b) - b\alpha^2 + a\beta^2 + b\gamma^2, \\ &4J(1+6b) - 4(a+2b) - b\alpha^2 - b\beta^2 - a\gamma^2] \end{aligned} \tag{52}$$